Journal Pre-proof

Te-rich Bi_2Te_3 thin films by electron−beam deposition: Structural, electrical, optical and thermoelectric properties

C. Sudarshan Conceptualization;Methodology;Investigation;Data curation;Visualization;Formal analysis;Writing - o
S. Jayakumar Resources;Formal analysis;Writing - review and editing;Supervision ,
K. Vaideki Supervision;Writing - review and editing ,
C. Sudakar Methodology;Resources;Formal Analysis;Writing - review and editing

PII: S0040-6090(20)30564-2
DOI: https://doi.org/10.1016/j.tsf.2020.138355
Reference: TSF 138355

To appear in: *Thin Solid Films*

Received date: 18 May 2020
Revised date: 17 September 2020
Accepted date: 18 September 2020

Please cite this article as: C. Sudarshan Conceptualization;Methodology;Investigation;Data curation;Visualization;F
S. Jayakumar Resources;Formal analysis;Writing - review and editing;Supervision ,
K. Vaideki Supervision;Writing - review and editing , C. Sudakar Methodology;Resources;Formal Analysis;Writing
Te-rich Bi_2Te_3 thin films by electron−beam deposition: Structural, electrical, optical and thermoelectric properties, *Thin Solid Films* (2020), doi: https://doi.org/10.1016/j.tsf.2020.138355

This is a PDF file of an article that has undergone enhancements after acceptance, such as the addition of a cover page and metadata, and formatting for readability, but it is not yet the definitive version of record. This version will undergo additional copyediting, typesetting and review before it is published in its final form, but we are providing this version to give early visibility of the article. Please note that, during the production process, errors may be discovered which could affect the content, and all legal disclaimers that apply to the journal pertain.

© 2020 Elsevier B.V. All rights reserved.

Highlights:

- Nanocrystalline Te-rich Bi_2Te_3 thin film is prepared by e^-–beam deposition at 300K.
- Vacuum annealing lead to intergrown Te-rich layers between the quintuples.
- Disordered planar structures are mostly concentrated on the crystallite surface.
- Seebeck coefficient becomes maximum (~ 97 μV/K) for the film annealed at 200 °C.
- Te-rich Bi_2Te_3 with $S^2\sigma$ ~29×10^{-4} W/K^2m is good for thermoelectric applications.

Journal Pre-proof

Te-rich Bi_2Te_3 thin films by electron–beam deposition: Structural, electrical, optical and thermoelectric properties

C. Sudarshan[a,*], S. Jayakumar[b], K. Vaideki[a], and C. Sudakar[c]

[a] Thin Film Centre, Department of Applied Science, PSG College of Technology, Coimbatore 641004, India

[b] Department of Physics, PSG Institute of Technology and Applied Research, Coimbatore 641062, India

[c] Multi-Functional Materials Laboratory, Department of Physics, Indian Institute of Technology Madras, Chennai 600036, India

***Corresponding author e-mail address: c.sudarshans@gmail.com**

Journal Pre-proof

Abstract: Tellurium-rich Bi_2Te_3 thin films are deposited by electron–beam evaporation technique at 300 K. These as-deposited thin films are further annealed at 100 °C, 200 °C and 300 °C for 1 h at a pressure of 3×10^{-4} Pa. X-ray diffraction (XRD) patterns of as-deposited films distinctly show Te phase along with Bi_2Te_3. Peak intensity ratio suggests the polycrystalline nature of as-deposited Bi_2Te_3 films. On vacuum annealing Te-rich Bi_2Te_3 films exhibit improved crystallinity with a *c*-axis preferred orientation. In addition, structural features related to Te and Bi_2Te_3 composition change with Te fraction diminishing on annealing at 300 °C. From Raman spectral studies, the presence of distinct Te-rich regions, predominantly within the interlayers of Bi_2Te_3, are discerned. Te becomes structurally integrated within the quintuples of Bi_2Te_3 lattice as intergrown layers. Disordered planar structures, mostly concentrated on crystallite surfaces result from Te accumulations as evidenced in high-resolution transmission electron microscopy lattice images and energy dispersive X-ray spectroscopy mapping. These are consistent with the observations from XRD and Raman studies further confirming Te-rich Bi_2Te_3 characteristics. Electrical properties of Te-rich Bi_2Te_3 thin films exhibit n-type semiconductor behaviour. Seebeck coefficient for as-deposited film is ~ 32 μV/K, which increases to ~ 97 μV/K on 200 °C annealing. Resistivity increases from 1.39×10^{-4} Ωcm to 18.76×10^{-4} Ωcm and power factor changes from 7.4×10^{-4} W/K^2m to 27.17×10^{-4} W/K^2m going through a maximum at 200 °C upon systematic annealing. Te-rich Bi_2Te_3 thin films annealed at 200 °C exhibit high

power factor (~ 29 × 10^{-4} W/K^2m) for a wide range of temperature gradients (ΔT from 30 °C to 165 °C).

Keywords: Tellurium rich bismuth telluride, Thin films, Electron–beam deposition, Seebeck Coefficient, Power factor.

1. Introduction

Bismuth telluride (Bi_2Te_3), a V-VI binary compound semiconductor, has a rhombohedral structure with space group $R\bar{3}m$. Due to the layered structure, it exhibits strong anisotropic properties in the bulk form. Thermoelectric properties of Bi_2Te_3 is shown to have a high figure of merit near room temperature. Hence, it is widely used as a device in integrated circuit [1], as heat pumps, and in thermoelectric devices [2]. Thin film form of Bi_2Te_3 also finds application in optoelectronics, electrochemical devices, sensors and photovoltaic solar cells [3-7]. Due to its favourable figure of merit near room temperature (ZT =1), bismuth telluride is being explored in thin film form for energy conversion applications [8]. The figure-of-merit of a thermoelectric material can be bettered by increasing electrical conductivity, increasing Seebeck coefficient, and decreasing thermal conductivity. Recently, epitaxial and highly crystalline Bi_2Te_3 thin films are extensively explored as a topological insulator or two-dimensional materials [9, 10]. While such efforts are blooming, the challenges for growing thin films for thermoelectric applications, i.e. preferably thick granular films with polycrystalline nature with better thermoelectrics properties are still prevailing [11]. Further, the role of defects in thin films is explored as the introducing dislocations through thermomechanical means in polycrystalline bulk thermoelectrics have led to crystallographic texture and densification, which in turn improve the thermoelectric properties [12]. For thin films, another big challenge is to measure and tailor the thermal conductivity changes. Therefore, significant focus is directed towards tailoring the power factor of thin films. In the last few decades, significant research interest is driven towards approaches which fine-tune the structure of material for the thermoelectric application. Experimental studies and theoretical calculations have shown that the nanostructured material provides significantly larger figure-of-merit values in the range of (ZT = 1 to 3) [13-20]. Methods to fabricate nanostructured materials have led a new class of thermoelectric system. With these nanostructured systems, ten to fifteen times increase in the figure-of-merit is already demonstrated [13]. The increase is mainly attributed to phonon

Journal Pre-proof

scattering at grain boundaries which lead to a significant reduction of phonon thermal conductivity [16, 21-23].

The preparation of stoichiometric bismuth telluride with a control on the formation of *n*-type and *p*-type characteristics in thin film forms are of substantial interest for their application in the integrated thermoelectric cooling used in microelectronic systems. The *n*-type Bi_2Te_3 thin films are of particular interest for integrated thermoelectric devices made by microfabrication process [24-27]. Z-H Zheng et al. [28] discussed the enhancement of carrier transport in the interface using organic and inorganic hybrid thermoelectric films. Also, the combinatorial effects of Pb doping and Cu deficiencies that enhance the transport characteristics were discussed by Y-H Zheng et al. [29]. It is well demonstrated that the stoichiometric Bi_2Te_3 crystals either can exhibit a *p*-type or *n*-type characteristics based on the type of point defects in the lattice. Most commonly, the *n*-type Bi_2Te_3 is found prominently when Te_{Bi} anti-site point defects are present, i.e. tellurium occupied bismuth lattice sites. It has been shown that the n-type characteristics acquired by the bismuth telluride can be obtained by increasing tellurium in Bi_2Te_3 [30-32]. The processes by which the n-type Bi_2Te_3 thin films have been obtained include electrochemical deposition [33], co-evaporation [34], co-sputtering [35], metal-organic chemical vapour deposition [36], pulsed laser deposition [37] and molecular beam epitaxy (MBE) [38, 39].

This manuscript reports on the growth of tellurium-rich Bi_2Te_3 thin films by electron beam (e-beam) deposition and investigate their properties. Composition control and stoichiometric deposition of Bi_2Te_3 thin films by e-beam evaporation were reported earlier[40]. However, the growth of Te-rich bismuth telluride thin films by this method is not known. In addition to depositing Te-rich Bi_2Te_3 polycrystalline thin films at room temperature vacuum annealing process is used to tailor their physical properties. This paper investigates the structural, morphological, optical and thermoelectric properties of these Te-rich Bi_2Te_3 thin films. Te-rich regions are shown to present predominantly as intergrowth layers within the interlayers of Bi_2Te_3 quintuples and are also seen concentrated on the crystallite surface. Te-rich Bi_2Te_3 is found to be more favourable for the thermoelectric application as it exhibits higher power factor compared to the stoichiometric Bi_2Te_3 films.

2. Experimental Procedure

Thin films of Te-rich Bi_2Te_3 are deposited by e-beam evaporation technique. The deposition system from HIND HI-VAC integrated with an e-beam power supply, and a high

Journal Pre-proof

Journal Pre-proof

vacuum diffusion pump was used. Bi_2Te_3 (Alfa Aesar 99.999%) loaded in the graphite crucibles placed in a water-cooled copper hearth serves as the source. The flux of Te and Bi during the e-beam evaporation can be altered by controlling the power to the electron gun [40]. A detailed presentation on the control of parameters for preparing stoichiometric, Bi and Te-rich Bi_2Te_3 films are reported elsewhere[40]. Near stoichiometric Bi_2Te_3 films are obtained by carrying out the deposition with specific power (67.5 W) applied to e-beam source and placing the substrates at the center of the holder. For obtaining Te-rich Bi_2Te_3 composition, a source power of 90 W was used. For the current study, the Te-rich Bi_2Te_3 films were coated on glass substrates placed at the centre of the substrate holder. Post-deposition annealing of these as-deposited Te-rich Bi_2Te_3 was carried out at 100 °C, 200 °C and 300 °C for 1 h under a pressure of 3×10^{-4} Pa. No other alterations such as using tellurium vapour were used during vacuum annealing.

The deposited thin films are studied for the structural and phase formation by X-ray diffractometer (X'pert-pro PANalytical) under a glancing angle mode with Cu K_α radiation (operating at 4 kW power; λ = 1.5406 Å). The scan was typically conducted in the 2θ ranges of 10° to 70° with a step size of ~ 0.01° at room temperature. Rietveld refinement of X-ray diffraction (XRD) patterns was carried out by using the software provided by X'pert Highscore. The morphological studies were carried out by obtaining secondary electron signals in a field emission scanning electron microscope (FESEM operated at 30 keV; FEI Quanta FEG 200/FEG 400). The thickness of the films is estimated from the cross-sectional secondary electron FESEM images. Energy-dispersive X-ray Spectroscopy (EDS) were acquired using the Bruker X Flash 6 I 10 detector (area 10 mm^2 ; energy resolution of ~129 eV) present in the FESEM. The Bi and Te concentration in the films are estimated with an uncertainty of ~0.5 *at.*%. Both bright field and high-resolution images, and electron diffraction are obtained on the samples collected from thin films using a transmission electron microscopy (TEM; JEOL JEM 2100) operating with an e-beam acceleration voltage of 200 kV. EDS mapping was carried out using a sub-nm e-beam probe available in the scanning TEM (STEM) mode of FEI Titan microscope operating with a 300 keV X-FEG high-brightness Schottky field emission source. ChemiSTEM Technology with Super-X 4-SDD, windowless EDAX detector system was used to acquire EDS maps. Atomic force microscopy (AFM; NT-MDT, Russia) was used to obtain surface topographic profiles in a tapping mode and roughness information. Diffuse reflection spectra (DRS; Perkin Elmer 2 plus) obtained in the 500 to 4000 cm^{-1} range, was used to estimate the optical bandgap.

Journal Pre-proof

Carrier concentration and mobility are estimated from Hall measurement made using (ECOPIA; HMS-3000). Resistivity (ρ) measurements were carried out at room temperature using a home-built four-probe resistivity measurement device comprising of a Keithley 2400 current source meter. Raman spectra were obtained using a micro-Raman spectrometer (Horiba Jobin-Yvon HR800 UV). The excitation wavelength of λ=488 nm line from the Ar ion laser was used as a source. Seebeck coefficient was measured on thin films (coated on 7.5 cm × 1cm glass substrates) using a home-built setup. The hot end of a copper block maintained by a temperature-controlled resistive heater and the cold end of another copper block maintained by cold water (4 °C) circulating through it were used to create temperature gradient (ΔT ~ 30 °C to ~165 °C) at two ends of the thin films. Making use of good thermal and electrical contacts, ΔT and Seebeck voltage ΔV were measured at points separated by 5 cm from the center of the film. The Seebeck coefficient (S) was calculated from the ratio ΔV/ΔT. Finally the thermoelectric power factors are estimated using S and ρ.

3. Result and Discussion:

3.1 X-ray diffraction:

Figure 1 (a) shows the XRD patterns of Te-rich Bi_2Te_3 thin films. XRD data from standard powder diffraction files for Bi_2Te_3 (ICDD # 015-0863) and Te (ICDD#065-3370) are also presented in Figure 1(a). While these two patterns have significant overlap, few distinct peaks can be used to differentiate the Te and Bi_2Te_3 phases. For example the peaks at 2θ ~ 23°, 38° and 40.3° can be used to differentiate these phases. The tellurium phase exhibits X-ray reflections at 2θ ~ 23.11°, 27.45°, 38.31° and 40.34° which are assigned to (100), (101) (102) and (110) planes, respectively. Whereas, Bi_2Te_3 phase show peaks at 2θ ~ 27.61°, 37.89°, 41.17°, 44.61°, 50.29°, 57.19° and 62.66° which correspond to (015), (10 10), (110), (10 15), (205), (210) and (02 13) planes. The XRD patterns of as-deposited thin films clearly show distinct Te diffraction peaks along with the Bi_2Te_3 phase. This indicates a possible Te-rich Bi_2Te_3 phase in the as-deposited films. Poor crystallinity of the as-deposited films is also evident from the broad peaks. Despite all this, it is interesting to see that the as-deposited films show reflections that are characteristic of the presence of nanocrystallites. In our previous study on the stoichiometric Bi_2Te_3 thin films by the same process, we have observed that the coated films tend to get preferentially orientated along (110) planes upon annealing [40]. On the contrary, the peak intensity ratio in these Te-rich Bi_2Te_3 films suggests that the films have polycrystalline nature with no preferred orientation. The structural

Journal Pre-proof

features with respect to Te and Bi_2Te_3 composition seem to change on post-annealing treatment under vacuum. This is clearly discernible in the 2θ range between 38° and 41°, and between 15° and 25°. However, unlike in the stoichiometric Bi_2Te_3 thin films [40], noticeable change in the relative intensity of diffraction peaks ~ 27.6° (015) and ~ 41.17° (110) indicating the preferential orientation of crystallites are not seen in the Te-rich Bi_2Te_3. The intense (015) reflection with the relative intensity of I(015)/I(10 10) similar to the polycrystalline phase is always seen suggesting the absence of (110) oriented crystallites. With annealing the intensity of Te peaks at 38.3° and 40.3° decrease and completely disappears in the 300 °C annealed thin films (refer to the dotted vertical lines in Fig. 1a).

The significant mismatch between the refined and the experimental data seem to emerge with annealing temperature. Specifically, the low intense peaks, seen around 2θ ~ 17°, 23° and ~ 38°, becomes challenging to be refined entirely as evident in 200 °C annealed thin film XRD data. This indicates the presence of a small fraction of Bi_xTe_y secondary phase segregation possibly within the Bi_2Te_3 lattice [35, 41]. Such secondary phase could result due to the recrystallization, evaporation and Te reaction with the Bi_2Te_3 phase. The crystallographic rearrangement taking place during such reaction, schematically represented in Fig.2, may lead to the formation of minor secondary phases, such as Bi_xTe_y, as found in films annealed at 100 °C and 200 °C. Structural similarities between Bi_2Te_3, Te and Bi provide ample opportunity for Te and Bi to intergrow within Bi_2Te_3 crystallites. For example, the stability of Bi layers coexisting between Bi_2Te_3 layers are shown by Fornari et al. [42] in a controlled growth carried out by MBE method. We contemplate in the present study, Te layers intergrow between Bi_2Te_3 layers with possible insertion of Te within the lattice (Fig. 2). As discussed in detail from the following sections on Raman spectroscopy and high-resolution transmission electron microscopy (HRTEM) with EDS mapping, we provide evidence which suggests that in fact, the Te-rich regions in the Bi_2Te_3 crystal structure prevail as intergrown features.

The occurrence of such secondary phases also influence the intensities of the Bi_2Te_3 X-ray reflections specifically (10 10), (00 15) and (02 13) planes as can be discerned 300 °C annealed thin films. The c-plane orientation of the film growth along the substrate surface on annealing is also observed from the emergence of relatively intense reflections from (006), (00 15) atomic planes. The (110) reflection intensity also decreases significantly indicating that this plane is oriented perpendicular to the substrate. In thin films, the preferential

Journal Pre-proof

Journal Pre-proof

orientations of grains strongly influence the X-ray intensity significantly. The crystallites exhibit intense reflections for certain (hkl) planes over the other. Due to this, few peaks do not get fitted well in the refinement as seen in 200 °C XRD data. Incorporating crystallites with certain preferential orientation as two different phases yield relatively best fit for the XRD data. Due to weak signal to noise ratio or possibly due to the growth of Te phase in Bi_2Te_3 lattice with preferential orientation, it is a bit difficult to get refined without feeding the preferential orientation direction for Te phase. Since the quality of the signal to noise ratio from the X-ray diffraction data are poor for the fitting, typical of thin film samples, we could not fit a few low intense peaks. For thin films, in general, the X-ray diffraction intensity is of low signal to noise ratio, despite the data acquired using glancing angle configuration with a high power X-ray source (4 kW rotating anode). Thus, the Te-rich Bi_2Te_3 thin film growth suggests that crystallites have relatively preferred orientation, i.e. c-plane parallel to the substrate surface [43].

The experimental data with Rietveld refinement fits are shown in Figure 1(a). The fitted parameters, including lattice constants *a* and *c*, and the particle size estimated from the refinement, are provided in Table 1. The plots of lattice parameters *a* and *c*, and c/a ratio *vs* annealing temperature are given in Figure 1(b). The lattice parameters of as-deposited films are a = 4.3749 Å and c = 30.0027 Å. On annealing, the change in the lattice parameters of *a* is seen to be minimal (~ 0.1 Å) for temperatures up to 200 °C. Beyond this, the lattice parameter *a* decreases. In contrast, lattice parameter *c* increase gradually and the net change in the lattice parameter between the as-deposited and 300 °C annealed thin films is ~ 0.56 Å. These values are slightly more than the cell parameters corresponding to the bulk Bi_2Te_3, a = 4.3858 Å and c = 30.4255 Å. Further, the Rietveld refinement of the as-deposited thin film shows the ratio of Bi_2Te_3 to Te phase to be around 70:30. With annealing, the Te content decreases mainly due to the evaporation or reaction with the Bi_2Te_3. Thus the changes observed in the Bi_2Te_3 lattice parameters (Figure 1b) can be correlated to the formation of the Te-rich Bi_2Te_3 phase. The average crystallite size estimated from the refinement of the film shows an increase from 130 Å for the as-deposited film to 233 Å for the film annealed at 300 °C.

3.2 Raman spectroscopy:

Bulk Bi_2Te_3 with layered rhombohedral structure (space group $R\bar{3}m$) and five-atom primitive cell exhibit 15 lattice vibrational modes, of these, three are acoustic, and twelve are

Journal Pre-proof

optical phonons. [44] Irreducible representation of modes by group theory on Bi_2Te_3 with inversion symmetry allow twelve optical branches ($2A_{1g}$, $2E_g$, $3A_{1u}$ and $3E_u$ symmetry) which are either Raman active or IR active [44]. Figure 3(a) presents the Raman spectra of Te-rich as-deposited and annealed Bi_2Te_3 thin films. The Raman shift of the obtained peaks and the corresponding mode assignment are listed in Table 2. The magnified regions of Raman spectra of Te-rich Bi_2Te_3 films are shown in Figure 3(b). Three characteristic modes ~ 98-99 cm^{-1} (E_g^2), 117 -119 cm^{-1} (A_{1u}) and 137- 139 cm^{-1} (A_{1g}^2) are clearly discerned in these spectra. The $E_g^1$and A_{1g}^1vibrations occur at lower frequencies than E_g^2 and A_{1g}^2. In all thin films both E_g^1 and A_{1g}^1 modes are not visible.

Both E_g and A_{1g} modes have twofold degeneracy. The mode E_g arise from the symmetric in-plane bending vibration in the same direction of -Te-Bi- atoms. The A_{1g} mode arises from the symmetric out-of-plane stretching vibration [45, 46]. The presence of E_g^2 and A_{1g}^2 modes in the as-deposited films indicate that the outer Bi and Te atoms move in opposite phase. This further confirms the presence of Bi_2Te_3 phase in the as-deposited film. In addition to these modes the presence of A_{1u} peak around 117 cm^{-1} in the as-deposited film suggests the presence of excess Te in the sample [47].

It is noteworthy to observe the decrease in the intensity of E_g^2 mode with the increase in annealing temperature. In addition to this, we also see a slight increase in the intensity of A_{1g}^2 mode. These observations indicate a more sensitive nature of out-of-plane vibrations than in-plane modes of vibrations. On the other hand, the observation of large A_{1u} peak intensity compared to E_g^2 and A_{1g}^2 indicates the presence of tellurium-rich Bi_2Te_3 crystallites in the samples. From Table 2 we can see a blue shift of A_{1u} (117.81 to 119.42 cm^{-1}) mode with annealing temperature. Beyond 200 °C of annealing the mode shift back to the original peak position. From this, we infer that the Bi-Te atoms vibrate along c-axis, i.e. perpendicular to the layers, due to small thickness of the films. The A_{1g}^2 modes initially blue shifts (from 137.73 to 139.69 cm^{-1}) on annealing at 100 °C and remains same till 200 °C. At annealing temperature of 300 °C there is a blue shift in both the modes A_{1u} (119.42 to 117.80 cm^{-1}) and A_{1g}^2 (139.69 to 138.19 cm^{-1}) compared to as-deposited film. The existence of blue and redshifts in Raman spectra indicate that quantum confinement effect and interlayer interaction between nanostructured Bi_2Te_3 layers dominate [45]. Further the inhomogeneous broadening of E_g^2 indicates a strong electron-phonon interaction between the nanoparticles

Journal Pre-proof

and causes the strain in the films. From figure 3(b) the line (or integrated) intensity ratio of I(A_{1g}^2)/I(E_g^2) and I(A_{1u}) /I(E_g^2) can be used to determine the number of quintuples in the Bi_2Te_3 films[48]. From Table 2, the ratio is high for 200 °C annealed films indicating the high density of quintuples occurring in the films. It is interesting to note that the full width at half maximum of A_{1u} decrease with the annealing up to 200 °C. At 300 °C the decrease in the ratio of I(A_{1g}^2)/I(E_g^2) and I(A_{1u})/I(E_g^2) and sudden increase in the broadening of A_{1u} suggests the breaking of quintuples. This result along with (006), (015), (10 10), (00 15) oriented growth in the 300 °C annealed sample suggests that the breaking of quintuples leads to the formation of tellurium rich crystallite surface. The strongest A_{1u} mode, seen at 300 °C in Raman spectra, suggests that the crystallographic rearrangements of the planes with tellurium rich crystallites layers. The films annealed ≤ 200 °C also showing the A_{1u} mode with lower intensity and with the inference from the XRD on the presence of Te crystallites suggests that the Te rich intergrown layers are becoming more and more with annealing. Thus, from Raman spectral studies it is concluded that the Te is present predominantly as a secondary phase between the Bi_2Te_3 crystallites and becomes integrated with the bismuth telluride lattice, most probably as intergrown Te-rich layers between the quintuples.

3.3 Scanning electron microscopy:

The surface morphological and cross-sectional FESEM images of Te-rich Bi_2Te_3 films are shown in Figure 4. The as-deposited film shows uniform surface topography. The thickness of the film is uniform (~ 500 nm) and reduces slightly to 473 nm on annealing at 300 °C. Thus annealing under high vacuum does not modify the film thickness significantly. All the film surfaces are made of nanocrystalline particles. Few regions show agglomerations leading to submicron-sized clusters composed of crystallites less than a few tens of nanometer. Despite the polycrystalline nature of thin films, the nanosized grains are expected to be mostly single crystallites. The HRTEM studies presented in the following section further confirm the single crystalline nature of the Bi_2Te_3 particles. Hence, mostly Bi_2Te_3 thin films form by an island-growth mechanism [49].

Annealing promotes the growth of the nanoscale grains, and some nanocrystals with size in the range of 10 to 100 nm emerge on the surface of the thin films as shown in Figure 4 (e to h). As the annealing temperature increases, the size and density of the nanocrystals increase[50], which could result in enhanced surface roughness. Thus, from FESEM studies, we infer that uniform crystallites are formed for the Te-rich Bi_2Te_3 phase. From the cross-

Journal Pre-proof

sectional SEM images, the thickness of as-deposited and annealed films are estimated (Table 3). The compositions of the films are also found from the EDS spectra (not shown). The estimated values confirm that all the films exhibit tellurium rich composition (Table 3). We believe that a small amount of Te evaporation occurs with annealing. The Te-rich composition from the EDS for 100 °C and 200 °C suggest the diffusion of Te to the surface on vacuum annealing. On 300 °C annealing, due to the high saturated vapour pressure of elemental Te, a slight decrease in the surface composition of Te compared to the thin films annealed < 200 °C are noted.

3.4 Atomic force microscopy:

The AFM images of Te-rich Bi_2Te_3 thin film surfaces are shown in Figure 5(a to d). Roughness values are estimated from the surface profiles. The result clearly shows an increase in roughness of thin films with annealing temperature. Furthermore, the surface of the films has wavy surface topography. The peak profiles indicating the grain protrusions above the surface are less pronounced over the valley regions. In the as-deposited film, the grain distribution is very uniform all over the surface. The as-deposited and 100 °C annealed thin films show larger grains resembling vertically standing boulder. These grains comprise of a large number of crystallites with size ~ 20 to 30 nm. On further annealing, the density of this boulder-like island grains reduces but grows larger in size, indicating the agglomeration of the crystallites. Due to this, the roughness of the films increases (Table 3) as the annealing is carried out from 100 °C to 300 °C. These noticeable changes seen in the surface topographic could result from the defects in the crystal system due to excess tellurium, the formation of pinholes and slightly lower density of films compared to the as-deposited film.

3.5 Transmission electron microscopy:

Particle size and phase distribution of Te-rich Bi_2Te_3 samples are investigated from bright-field TEM images obtained using a JEOL JEM 2100 microscope. The bright-field images of all the thin films are shown in Figure 6 (a-d), and the corresponding selected area electron diffraction (SAED) films are shown in Figure 6(e –h). All the bright field images show the agglomerates of nanocrystalline particles. The agglomerated chunk of particles seen in the TEM is due to the way the TEM samples were prepared. The scrapped particles are transferred to the Cu-grids coated with the carbon layer. In all these big chunks the edges are e-beam transparent and show the particles are composed of nanocrystalline grains. The

Journal Pre-proof

Journal Pre-proof

SAED pattern from these samples shows spotted ring patterns further substantiating the single crystalline nature of nanoparticles. The SAED in all cases matches well with the simulated pattern made using Bi_2Te_3 CIF files.

It should be noted that the distinction of any Te from the SAED pattern will be difficult as this phase overlaps a lot with the pattern from Bi_2Te_3. Most importantly, we infer that the crystallites are characteristics of Bi_2Te_3 phase from the TEM and SAED studies. We also carried out the HRTEM lattice images from the nanocrystallites seen in the samples. These images are shown in Figure 7. All the lattice fringe *d* spacing can be correlated to the Bi_2Te_3 lattice planes. The corresponding indexing is given in the same figure (Figure 7). While the lattice planes are found to be perfect within the core of the crystallites, the grain boundary and surface regions show the presence of planar defects. As an example, the HRTEM image of 300 °C annealed samples taken at the edge of a crystallite is shown in the inset of Figure 7(d). The lattice planes are wrinkled, and extra planes get interspersed with the core lattice. Such disorders found to be more on the surface is consistent with the observation from the previous characterization that the Te gets accumulated at the surface of the crystallites.

We carried out elemental EDS mapping using sub-nm e-beam probe in STEM mode. Representative data carried out on Te-rich Bi_2Te_3 samples vacuum annealed at 100 °C and 200 °C thin film specimens are shown below. In Figure 8 (panel (A)), EDS mapping shows a significant difference in the intensity distribution of Bi and Te X-rays emitted from the particle, suggesting that the Te is rich on one end of the crystallite region. Even in thin films vacuum annealed at 200 °C, we find Te-rich regions from the surface of the particles as well as in the interface region between two particles, clearly evident as shown in the EDS maps and line scan data given in the panels (B) and (C) of Figure 8. While it becomes difficult to distinguish the Te-rich regions based on the intensity distribution of X-ray counts in the EDS maps, the line scan carried out across regions clearly show Te-rich regions. Thus, from HRTEM and EDS mapping images, Te regions Bi_2Te_3 becomes very evident.

3.6 Diffuse reflection spectroscopy:

Diffuse reflection spectra of all the thin films obtained over a wide range of spectral regions spanning from 500 cm^{-1} to 4000 cm^{-1} are shown in Figure 9(a). The variation of % reflection occurs in the films due to the surface charge carrier and grain size. In all the films,

Journal Pre-proof

Journal Pre-proof

a maximum reflection is seen around 1250 cm^{-1}. For 200 °C annealed thin films, the diffuse reflection is found to be half that of the rest of the films. It is noteworthy that around this annealing temperature, the crystallites structurally reorient as evidenced from the various techniques discussed above. This might affect the diffuse reflection drastically due to the surface morphological changes. Otherwise, the changes in the reflection features as a function of wavelength are found to be similar to that of other Bi_2Te_3 thin films. It has been reported to be a direct (~ 0.13 eV) as well as an indirect bandgap (~ 0.21 eV) material [51, 52]. In our studies, we calculated both direct and indirect bandgap values using Kubelka-Munk (K-M) function. The DRS data is converted to Kubelka-Munk function F(R), which is equivalent to the absorption coefficient. The plots $[F(R)h\nu]^2 \propto (h\nu - E_g)$ and $[F(R)h\nu]^{1/2} \propto (h\nu - E_g)$ are made as shown in Figure 9 (b and c). The direct bandgap values increase linearly changing E_g from 0.109 eV for as-deposited Bi_2Te_3 to 0.118 eV for 200 °C annealed thin films. With further annealing at 300 °C E_g decreases to 0.109 eV. The decrease in value for 300 °C annealed film shows that there is a change in structure, microstrain and dislocation densities of the film during annealing, the indication of which also reflected in our XRD results. All the films show the bandgap value ~ 0.11 eV, which is consistent with the theoretical values reported by Mishra et al. [53, 54]. The estimated indirect bandgap values show a similar trend, but the values are (~ 0.02 to 0.06 eV) lower than the values reported in the literature [55].

3.7 Electric and Thermoelectric Properties:

The carrier concentration (n) and mobility (μ) estimated from Hall voltage and resistivity of as-deposited and annealed thin films are shown in Fig. 10. The Hall coefficient of all the samples is negative, implying the n-type semiconductor characteristics of thin films. On annealing the films under high vacuum, carrier concentration values increase from 2.43 × 10^{21} cm^{-3} for as-deposited thin films to 4.57 × 10^{21} cm^{-3} for thin films annealed at 200 °C. The carrier concentration rapidly falls to 0.28 × 10^{21} cm^{-3} on further annealing the films at 300 °C. The change in carrier concentration could result due to various factors, including the interdiffusion of Bi and Te, reduction of defect vacancies and improved crystalline quality [49]. Such a change could also be due to the microstructure, which reflects in the XRD and Raman results. In Te-rich Bi_2Te_3, the excess Te occupying the Bi site can give rise to free-electron charge carriers according to the following equation:

$$Te + Bi_{Bi} = Te_{Bi}^{+} + Bi + e^{-}$$

Journal Pre-proof

The increase in the charge carrier concentration with vacuum annealing process suggests that excess Te in the thin films react with Bi_{Bi} more at a higher temperature. At 300 °C the drastic decrease in the carrier concentration might result from the significant evaporation of Te from the films. The annealing temperature-dependent variation of carrier mobility and carrier concentration exhibit the opposite trend [56]. Carrier mobility is found to be high ~ 16 cm^2/Vs at 300 °C. Better recrystallization of the Bi_2Te_3 grains with reduction of grain boundaries and aggregation of the nanocrystallites, and minimization of defects in the lattice could facilitate easy current flow.

Electrical resistivity *vs* temperature measured from 30 °C to 200 °C for the as-deposited and annealed thin films are shown in Figure 11. The electrical resistivity varies linearly with the temperature. Moreover, the temperature coefficient of the electrical resistivity is, in general, negative for all the thin films suggesting the presence of strongly non-degenerate carries [57]. The electrical resistivity of the film annealed at 300 °C varies linearly from ~ 19 × 10^{-4} to 9 × 10^{-4} Ωcm as the temperature increases. Compared to low temperature (< 200 °C) annealed films, the resistivity is at least one order more for the 300 °C annealed films. Due to Te evaporation, reduction of Te in the crystallites can affect the conductivity largely. However, it should be noted that the resistivity of Te-rich thin films prepared by co-evaporation technique is found to be one order more than the Bi-rich Bi_2Te_3 reported by Zou et al. [34]. Reports by Kim et al. also suggest increased resistivity with Te-rich Bi_2Te_3 [35]. Our results are consistent with these reports, and the large resistivity could be a true effect of Te replacing Bi in the Bi_2Te_3 lattice. The less variation of resistivity for the films annealed ≤ 200 °C shows that the poor electron scattering domination due to excess Te crystallites.

The activation energy is estimated using the relation $\ln(\sigma) = \ln(\sigma_0) - (E_a/K_BT)$, where σ_0 is the temperature-independent conductivity, E_a is the activation energy in joules, K_B is Boltzmann constant and T is the absolute temperature. E_a varies from 0.033 to 0.044 eV for the films annealed ≤ 200 °C and increases to 0.068 eV for the 300 °C annealed thin films. The increase in activation energy shows that the grain boundaries are significantly disordered (see HRTEM images in Fig. 7d). The electron scattering at these distorted grain boundaries requires considerable energy for the electron to transport. The accumulation of

charges in these grain boundaries is directly correlated to the energy barrier as proposed by Slater [58].

Figure 12 shows the resistivity, Seebeck coefficient, and power factor of Te-rich Bi_2Te_3 films measured at 300 K. The negative value of the Seebeck coefficient found for all the thin films indicate *n*-type semiconductor characteristics. The Seebeck coefficient for the as-deposited thin film is ~ 32 μV/K. This increases to a maximum of ~ 97 μV/K for 200 °C annealed thin films. Seebeck coefficient reduces to ~ 64 μV/K for 300 °C vacuum annealed film. The power factor is calculated using the relation S^2/ρ. The power factor of as-deposited films is found to be ~ 7 × 10^{-4} W/K^2m and increases to ~ 27 × 10^{-4} W/K^2m for the 200 °C annealed thin films. This value is fivefold larger than the one measured on near-stoichiometric Bi_2Te_3 thin films in our previous work [40]. Also, these values are higher than the reported values [34, 59-66] and also almost matches with the power factor values of the Bi_2Te_3 films deposited at higher temperature [34, 49, 63, 67, 68]. In 300 °C annealed thin films, power factor sharply decreases to ~ 2 × 10^{-4} W/K^2m. This may be due to the loss of Te in the thin film on high-temperature treatment under low-pressure ambient. Thus the power factor seems to get influenced by the presence of Te-rich conditions in the thin films.

The power factor is also estimated by measuring the Seebeck coefficient at high temperature gradients (ΔT). The Seebeck coefficient values for all the films show a decreasing trend with increasing temperature (Figure 13a). The power factor remains almost constant for all the ΔT measured between 30 °C and 165 °C (Figure 13b). Power factor ~ 28× 10^{-4} W/K^2m found in the 200 °C vacuum annealed thin films is the maximum value we found in this set of samples. For the thin films where the secondary phase is discerned, i.e. Te crystallites found in the as-deposited and Te loss discerned in 300 °C vacuum annealed thin films[69], the power factor is found to be small even though measured at high ΔT. Thus, loss of tellurium in the thin films lower power factor as found in the case of high temperature annealed Te-rich Bi_2Te_3 film (300 °C).

This demonstrates that optimization of annealing (~200 °C) under high vacuum is required to achieve a favorable microstructure and composition in Bi_2Te_3 thin films. Such tailorable electrical properties, thus, resulting larger power factor are demonstrated in e-beam deposited thin films. To conclude, the power factor is shown to significantly depend on the composition of thin film, i.e. Te-rich conditions, in addition to the processing conditions that

Journal Pre-proof

require to be tailored. Therefore, the power factor and hence the thermoelectric properties of bismuth telluride thin films are shown to have large influence by the growth mechanism of Te-rich Bi_2Te_3 crystallites.

4. Conclusion

The nanocrystalline Te-rich Bi_2Te_3 thin films are fabricated at ambient temperature (~30 °C) using e-beam evaporation technique. From XRD, EDS and Raman studies it is confirmed that the films are Te-rich Bi_2Te_3. HRTEM studies suggest that the disorders resulting in the lattice planes are found to be more on the crystallite surface. These disorders are due to Te getting accumulated at the surface of the crystallites. Excess Te present in the as-deposited films gets interspersed into the Bi_2Te_3 crystallites and becomes disordered planar defects leading to intergrown Te-rich layers between quintuples. Such Te-rich regions are seen on the grain surfaces. Due to these interesting compositional and microstructural features, Te-rich Bi_2Te_3 thin films exhibit properties most suitable for thermoelectric applications. The electrical properties of the nanocrystalline thin films exhibit n-type semiconductor behaviour. The Seebeck coefficient changes with annealing conditions: ~ 32 μV/K for as-deposited films and a maximum value ~ 97 μV/K found in 200 °C annealed thin films. The electrical resistivity increases from 1.39×10^{-4} Ωcm to 18.76×10^{-4} Ωcm with annealing temperature. Power factor measured at room temperature lies in the range of $7.4 \times 10^{-4}\ W/K^2m$ to $27.17 \times 10^{-4}\ W/K^2m$ as the annealing temperature varies from 30 °C to 300 °C. The effect of applied temperature for creating large ΔT on thermoelectric properties suggest that 200 °C annealed thin films exhibit high power factors (~ 29 x 10^{-4} W/K^2m) and is favourable for thermoelectric applications. From this work and a previous study (i.e. stoichiometric Bi_2Te_3 film) it ascertained that the thin film annealed at 200 °C under vacuum with suitable electrical and thermal properties are the appropriate choice for the thermoelectric application.

Journal Pre-proof

References

[1] M. Hines, J. Lenhardt, M. Lu, L. Jiang, Z. Xiao, Cooling effect of nanoscale Bi2Te3/Sb2Te3 multilayered thermoelectric thin films, Journal of Vacuum Science & Technology A: Vacuum, Surfaces, and Films, 30 (2012) 041509.

[2] C. Shafai, M.J. Brett, A micro-integrated Peltier heat pump for localized on-chip temperature control, Canadian Journal of Physics, 74 (1996) 139-142.

[3] D. Arivuoli, F.D. Gnanam, P. Ramasamy, Growth and microhardness studies of chalcogneides of arsenic, antimony and bismuth, Journal of Materials Science Letters, 7 (1988) 711-713.

[4] S.B. Riffat, X. Ma, Thermoelectrics: a review of present and potential applications, Applied Thermal Engineering, 23 (2003) 913-935.

[5] M.-Y. Kim, T.-S. Oh, Thermoelectric Characteristics of the Thermopile Sensors with Variations of the Width and the Thickness of the Electrodeposited Bismuth-Telluride and Antimony-Telluride Thin Films, Materials Transactions, 51 (2010) 1909-1913.

[6] M.-Y. Kim, T.-S. Oh, Thermoelectric Thin Film Device of Cross-Plane Configuration Processed by Electrodeposition and Flip-Chip Bonding, Materials Transactions, 53 (2012) 2160-2165.

[7] S. Herwaarden, Proc. 16th Int. Conf. on Thermoelectrics, DOI ((International Society of Thermoelectrics, 1997)) pp.47-55.

[8] D.M. Rowe, C.M. Bhandari, Modern thermoelectrics, Reston Pub. Co., Reston, Va., 1983.

[9] C.I. Fornari, E. Abramof, P.H.O. Rappl, S.W. Kycia, S.L. Morelhão, Morphology Control in van der Waals Epitaxy of Bismuth Telluride Topological Insulators, MRS Advances, DOI 10.1557/adv.2020.202(2020) 1-7.

[10] Z. Liao, M. Brahlek, J.M. Ok, L. Nuckols, Y. Sharma, Q. Lu, Y. Zhang, H.N. Lee, Pulsed-laser epitaxy of topological insulator Bi2Te3 thin films, APL Materials, 7 (2019) 041101.

[11] M. Takashiri, Thin Films of Bismuth-Telluride-Based Alloys, in: P. Mele, D. Narducci, M. Ohta, K. Biswas, J. Morante, S. Saini, T. Endo (Eds.) Thermoelectric Thin Films: Materials and Devices, Springer International Publishing, Cham, 2019, pp. 1-29.

[12] D.L. Medlin, G.J. Snyder, Interfaces in bulk thermoelectric materials: A review for Current Opinion in Colloid and Interface Science, Current Opinion in Colloid & Interface Science, 14 (2009) 226-235.

Journal Pre-proof

[13] L.D. Hicks, M.S. Dresselhaus, Thermoelectric figure of merit of a one-dimensional conductor, Physical Review B, 47 (1993) 16631-16634.

[14] G. Chen, Thermal conductivity and ballistic-phonon transport in the cross-plane direction of superlattices, Physical Review B, 57 (1998) 14958-14973.

[15] D.A. Broido, T.L. Reinecke, Thermoelectric power factor in superlattice systems, Applied Physics Letters, 77 (2000) 705-707.

[16] R. Venkatasubramanian, E. Siivola, T. Colpitts, B. O'Quinn, Thin-film thermoelectric devices with high room-temperature figures of merit, Nature, 413 (2001) 597-602.

[17] D.G. Cahill, W.K. Ford, K.E. Goodson, G.D. Mahan, A. Majumdar, H.J. Maris, R. Merlin, S.R. Phillpot, Nanoscale thermal transport, Journal of Applied Physics, 93 (2003) 793-818.

[18] G. Chen, Diffusion–transmission interface condition for electron and phonon transport, Applied Physics Letters, 82 (2003) 991-993.

[19] D. Vashaee, A. Shakouri, Electronic and thermoelectric transport in semiconductor and metallic superlattices, Journal of Applied Physics, 95 (2004) 1233-1245.

[20] R. Yang, G. Chen, Thermal conductivity modeling of periodic two-dimensional nanocomposites, Physical Review B, 69 (2004) 195316.

[21] G.A. Slack, New Materials and Performance Limits for Thermoelectric Cooling, CRC Handbook of Thermoelectrics, DOI (1995) 407-440.

[22] M.S. Dresselhaus, G. Chen, M.Y. Tang, R.G. Yang, H. Lee, D.Z. Wang, Z.F. Ren, J.P. Fleurial, P. Gogna, New Directions for Low-Dimensional Thermoelectric Materials, Advanced Materials, 19 (2007) 1043-1053.

[23] A.L. Bassi, A. Bailini, C.S. Casari, F. Donati, A. Mantegazza, M. Passoni, V. Russo, C.E. Bottani, Thermoelectric properties of Bi–Te films with controlled structure and morphology, Journal of Applied Physics, 105 (2009) 124307.

[24] L.W. da Silva, M. Kaviany, Micro-thermoelectric cooler: interfacial effects on thermal and electrical transport, International Journal of Heat and Mass Transfer, 47 (2004) 2417-2435.

[25] U. Dillner, E. Kessler, H.G. Meyer, Figures of merit of thermoelectric and bolometric thermal radiation sensors, J. Sens. Sens. Syst., 2 (2013) 85-94.

[26] J. Zhang, W. Luan, H. Huang, Y. Qi, S.-T. Tu, Preparation and characteristics of Pt/ACC catalyst for thermoelectric thin film hydrogen sensor, Sensors and Actuators B: Chemical, 128 (2007) 266-272.

Journal Pre-proof

[27] Z.-H. Zheng, J.-T. Luo, T.-B. Chen, X.-H. Zhang, G.-X. Liang, P. Fan, Using high thermal stability flexible thin film thermoelectric generator at moderate temperature, Applied Physics Letters, 112 (2018) 163901.

[28] Z.-h. Zheng, P. Fan, J.-t. Luo, G.-x. Liang, H.-l. Ma, X.-h. Zhang, C. Yang, Y.Q. Fu, High-performance p-type inorganic–organic hybrid thermoelectric thin films, Nanoscale, 10 (2018) 13511-13519.

[29] Y.-X. Chen, K.-D. Shi, F. Li, X. Xu, Z.-H. Ge, J. He, Highly enhanced thermoelectric performance in BiCuSeO ceramics realized by Pb doping and introducing Cu deficiencies, Journal of the American Ceramic Society, 102 (2019) 5989-5996.

[30] M. Goto, M. Sasaki, Y. Xu, T. Zhan, Y. Isoda, Y. Shinohara, Control of p-type and n-type thermoelectric properties of bismuth telluride thin films by combinatorial sputter coating technology, Applied Surface Science, 407 (2017) 405-411.

[31] K. Park, K. Ahn, J. Cha, S. Lee, S.I. Chae, S.-P. Cho, S. Ryee, J. Im, J. Lee, S.-D. Park, M.J. Han, I. Chung, T. Hyeon, Extraordinary Off-Stoichiometric Bismuth Telluride for Enhanced n-Type Thermoelectric Power Factor, Journal of the American Chemical Society, 138 (2016) 14458-14468.

[32] I.T. Witting, J.A. Grovogui, V.P. Dravid, G.J. Snyder, Thermoelectric transport enhancement of Te-rich bismuth antimony telluride ($Bi_{0.5}Sb_{1.5}Te_{3+x}$) through controlled porosity, Journal of Materiomics, 6 (2020) 532-544.

[33] B.Y. Yoo, C.K. Huang, J.R. Lim, J. Herman, M.A. Ryan, J.P. Fleurial, N.V. Myung, Electrochemically deposited thermoelectric n-type Bi2Te3 thin films, Electrochimica Acta, 50 (2005) 4371-4377.

[34] H. Zou, D.M. Rowe, G. Min, Growth of p- and n-type bismuth telluride thin films by co-evaporation, Journal of Crystal Growth, 222 (2001) 82-87.

[35] D.-H. Kim, E. Byon, G.-H. Lee, S. Cho, Effect of deposition temperature on the structural and thermoelectric properties of bismuth telluride thin films grown by co-sputtering, Thin Solid Films, 510 (2006) 148-153.

[36] A. Giani, A. Boulouz, F. Pascal-Delannoy, A. Foucaran, E. Charles, A. Boyer, Growth of Bi_2Te_3 and Sb_2Te_3 thin films by MOCVD, Materials Science and Engineering: B, 64 (1999) 19-24.

[37] Z. Yu, X. Wang, Y. Du, S. Aminorroaya-Yamni, C. Zhang, K. Chuang, S. Li, Fabrication and characterization of textured Bi_2Te_3 thermoelectric thin films prepared on glass substrates at room temperature using pulsed laser deposition, Journal of Crystal Growth, 362 (2013) 247-251.

Journal Pre-proof

[38] S. Cho, Y. Kim, A. DiVenere, G.K. Wong, J.B. Ketterson, J.R. Meyer, Antisite defects of Bi_2Te_3 thin films, Applied Physics Letters, 75 (1999) 1401-1403.

[39] Y. Kim, S. Cho, A. DiVenere, G.K.L. Wong, J.B. Ketterson, Composition-dependent layered structure and transport properties in BiTe thin films, Physical Review B, 63 (2001) 155306.

[40] C. Sudarshan, S. Jayakumar, K. Vaideki, C. Sudakar, Effect of vacuum annealing on structural, electrical and thermal properties of e-beam evaporated Bi_2Te_3 thin films, Thin Solid Films, 629 (2017) 28-38.

[41] C.-J. Liu, G.-J. Liu, Y.-L. Liu, L.-R. Chen, A. B. Kaiser, Enhanced thermoelectric performance of compacted $Bi_{0.5}Sb_{1.5}Te_3$ nanoplatelets with low thermal conductivity, 2011.

[42] C.I. Fornari, P.H.O. Rappl, S.L. Morelhão, E. Abramof, Structural properties of Bi2Te3 topological insulator thin films grown by molecular beam epitaxy on (111) BaF2 substrates, Journal of Applied Physics, 119 (2016) 165303.

[43] S.-j. Jeon, M. Oh, H. Jeon, S. Hyun, H.-j. Lee, Effects of post-annealing on thermoelectric properties of bismuth–tellurium thin films deposited by co-sputtering, Microelectronic Engineering, 88 (2011) 541-544.

[44] W. Richter, C.R. Becker, A Raman and far-infrared investigation of phonons in the rhombohedral V_2–VI_3 compounds Bi_2Te_3, Bi_2Se_3, Sb_2Te_3 and $Bi_2(Te_{1-x}Se_x)_3$ ($0 < x < 1$), $(Bi_{1-y}Sb_y)_2Te_3$ ($0 < y < 1$), physica status solidi (b), 84 (1977) 619-628.

[45] H. Rui, W. Zhenhua, L.J.Q. Richard, D. Conor, B. Ben, T.E. Kidd, C.C. Chancey, P.A.G. Xuan, Observation of infrared-active modes in Raman scattering from topological insulator nanoplates, Nanotechnology, 23 (2012) 455703.

[46] P. Srivastava, P. Kumar, K. Singh, Crystal Symmetry Breaking in Few Quintuple Bi_2Te_3 Nanosheets: Applications in Nanometrology of Topological Insulators and Low-Temperature Thermoelectrics, Journal of Nanoscience and Nanotechnology, 14 (2014) 5856-5863.

[47] V. Russo, A. Bailini, M. Zamboni, M. Passoni, C. Conti, C.S. Casari, A. Li Bassi, C.E. Bottani, Raman spectroscopy of Bi-Te thin films, Journal of Raman Spectroscopy, 39 (2008) 205-210.

[48] K.M.F. Shahil, M.Z. Hossain, D. Teweldebrhan, A.A. Balandin, Crystal symmetry breaking in few-quintuple Bi_2Te_3 films: Applications in nanometrology of topological insulators, Applied Physics Letters, 96 (2010) 153103.

Journal Pre-proof

[49] J.X. Zhang, Q. Li, P.J. Niu, Q.X. Yang, B.M. Tan, X.H. Niu, B.H. Gao, Effect of annealing temperature on microstructure and thermoelectric properties of bismuth–telluride multilayer thin films prepared by magnetron sputtering, Materials Research Innovations, 19 (2015) S10-408-S410-412.

[50] J. Song, X. Chen, Y. Tang, Q. Yao, L. Chen, Post-annealing Effect on Microstructures and Thermoelectric Properties of Bi0.45Sb1.55Te3 Thin Films Depositedby Co-sputtering, Journal of Electronic Materials, 41 (2012) 3068-3072.

[51] I.G. Austin, The Optical Properties of Bismuth Telluride, Proceedings of the Physical Society, 72 (1958) 545.

[52] S. Biswas, R. Bhattacharya, Two Valence Subbands in Single Crystals of Bismuth Telluride Doped with Lead and Its Electrical Properties, physica status solidi (b), 151 (1989) 193-201.

[53] S.K. Mishra, S. Satpathy, O. Jepsen, Electronic structure and thermoelectric properties of bismuth telluride and bismuth selenide, Journal of Physics: Condensed Matter, 9 (1997) 461.

[54] E.H. Kaddouri, T. Maurice, X. Gratens, S. Charar, S. Benet, A. Mefleh, J.C. Tedenac, B. Liautard, Optical Properties of Bismuth Telluride Thin Films, Bi_2Te_3/Si(100) and Bi_2Te_3/SiO_2/Si(100), physica status solidi (a), 176 (1999) 1071-1076.

[55] S.D. Mahanti, P.M. Larson, D. Bilc, H. Li, Electronic Structure of Complex Bismuth Chalcogenide Systems, in: M.G. Kanatzidis, S.D. Mahanti, T.P. Hogan (Eds.) Chemistry, Physics, and Materials Science of Thermoelectric Materials: Beyond Bismuth Telluride, Springer US, Boston, MA, 2003, pp. 227-247.

[56] X. Wang, H. He, N. Wang, L. Miao, Effects of annealing temperature on thermoelectric properties of Bi_2Te_3 films prepared by co-sputtering, Applied Surface Science, 276 (2013) 539-542.

[57] H.J. Goldsmid, Heat Conduction in Bismuth Telluride, Proceedings of the Physical Society, 72 (1958) 17.

[58] J.C. Slater, Barrier Theory of the Photoconductivity of Lead Sulfide, Physical Review, 103 (1956) 1631-1644.

[59] D.-H. Kim, G.-H. Lee, Effect of rapid thermal annealing on thermoelectric properties of bismuth telluride films grown by co-sputtering, Materials Science and Engineering: B, 131 (2006) 106-110.

Journal Pre-proof

Journal Pre-proof

[60] Z.-h. Zheng, P. Fan, G.-x. Liang, D.-p. Zhang, X.-m. Cai, T.-b. Chen, Annealing temperature influence on electrical properties of ion beam sputtered Bi_2Te_3 thin films, Journal of Physics and Chemistry of Solids, 71 (2010) 1713-1716.

[61] Y. Deng, H.-m. Liang, Y. Wang, Z.-w. Zhang, M. Tan, J.-l. Cui, Growth and transport properties of oriented bismuth telluride films, Journal of Alloys and Compounds, 509 (2011) 5683-5687.

[62] Z.-k. Cai, P. Fan, Z.-h. Zheng, P.-j. Liu, T.-b. Chen, X.-m. Cai, J.-t. Luo, G.-x. Liang, D.-p. Zhang, Thermoelectric properties and micro-structure characteristics of annealed N-type bismuth telluride thin film, Applied Surface Science, 280 (2013) 225-228.

[63] J.-H. Kim, J.-Y. Choi, J.-M. Bae, M.-Y. Kim, T.-S. Oh, Thermoelectric Characteristics of n-Type Bi_2Te_3 and p-Type Sb_2Te_3 Thin Films Prepared by Co-Evaporation and Annealing for Thermopile Sensor Applications, Materials Transactions, 54 (2013) 618-625.

[64] M.M. Rashid, K.H. Cho, G.-S. Chung, Rapid thermal annealing effects on the microstructure and the thermoelectric properties of electrodeposited Bi_2Te_3 film, Applied Surface Science, 279 (2013) 23-30.

[65] Z. Zeng, P. Yang, Z. Hu, Temperature and size effects on electrical properties and thermoelectric power of Bismuth Telluride thin films deposited by co-sputtering, Applied Surface Science, 268 (2013) 472-476.

[66] K. Kusagaya, H. Hagino, S. Tanaka, K. Miyazaki, M. Takashiri, Structural and Thermoelectric Properties of Nanocrystalline Bismuth Telluride Thin Films Under Compressive and Tensile Strain, Journal of Electronic Materials, 44 (2015) 1632-1636.

[67] O. Vigil-Galán, F. Cruz-Gandarilla, J. Fandiño, F. Roy, J. Sastré-Hernández, G. Contreras-Puente, Physical properties of Bi_2Te_3 and Sb_2Te_3 films deposited by close space vapor transport, Semiconductor Science and Technology, 24 (2009) 025025.

[68] L.M. Goncalves, C. Couto, P. Alpuim, A.G. Rolo, F. Völklein, J.H. Correia, Optimization of thermoelectric properties on Bi_2Te_3 thin films deposited by thermal co-evaporation, Thin Solid Films, 518 (2010) 2816-2821.

[69] K. Singkaselit, A. Sakulkalavek, R. Sakdanuphab, Effects of annealing temperature on the structural, mechanical and electrical properties of flexible bismuth telluride thin films prepared by high-pressure RF magnetron sputtering, Advances in Natural Sciences: Nanoscience and Nanotechnology, 8 (2017) 035002.

Journal Pre-proof

Figure 1: (a) X-ray diffraction data for the as-deposited and post annealed Te-rich Bi_2Te_3 thin films. Rietveld refinements of the XRD data are also shown in the plots. The measured intensities and the Rietveld patterns are shown in black and red colour lines, respectively. The vertical dotted lines are guide to eye to infer the peak positions. (b) Lattice parameters *a*, *c* and *c/a* ratio of as-deposited and post annealed Te-rich Bi_2Te_3 films are shown as a function of annealing temperature.

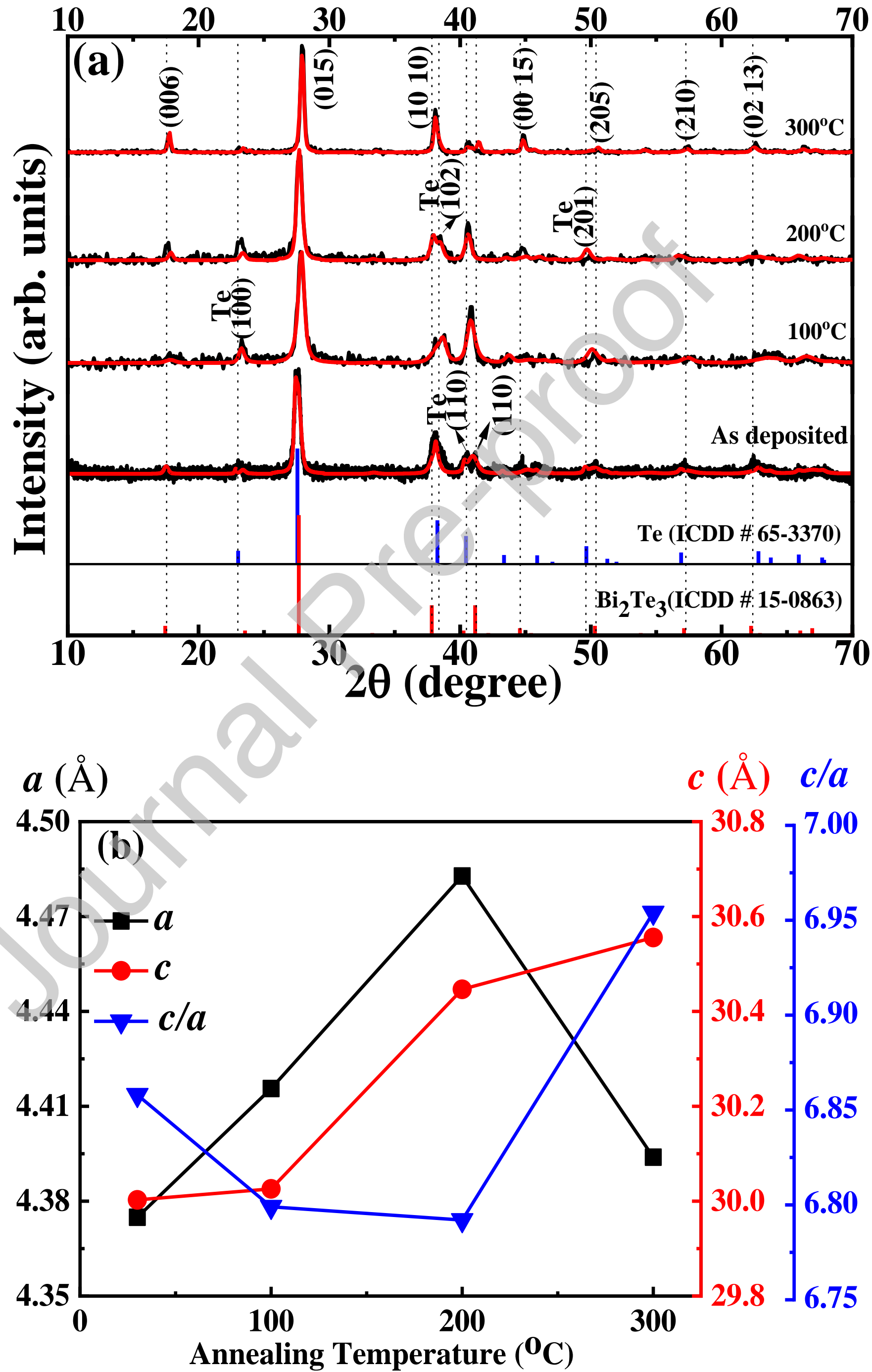

Journal Pre-proof

Figure 2: Schematic representation of structural evolution of e-beam evaporated Te-rich Bi_2Te_3 thin films as a function of annealing temperature.

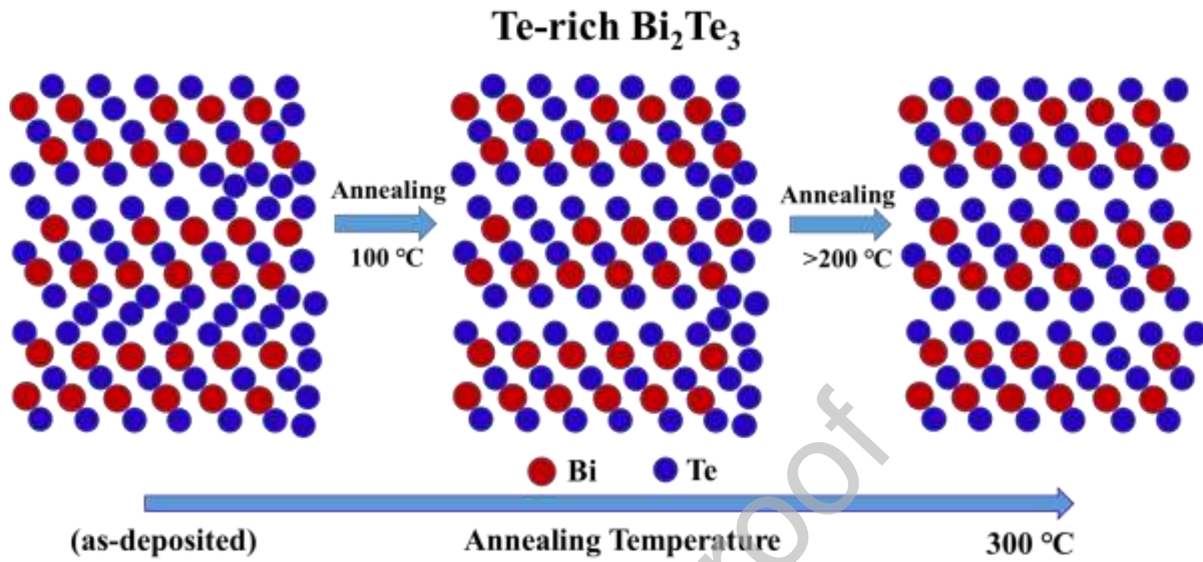

Journal Pre-proof

Figure 3: Raman spectra acquired with an excitation wavelength 488 nm on samples of as-deposited and post annealed Te-rich Bi_2Te_3 films. (a) Raman spectra in the wavenumber region between 75 cm^{-1} to 1050 cm^{-1} is shown. (b) E_g^2, A_{1u} and A_{1g}^2 modes are shown using the magnified region between 75 cm^{-1} to 175 cm^{-1} from spectra given in (a). The spectra is fitted with Gaussian-Lorentzian peak profiles, shown in blue (E_g^2), red (A_{1u}) and brown (A_{1g}^2). The data are shown in symbol and the fitted profile is shown in line.

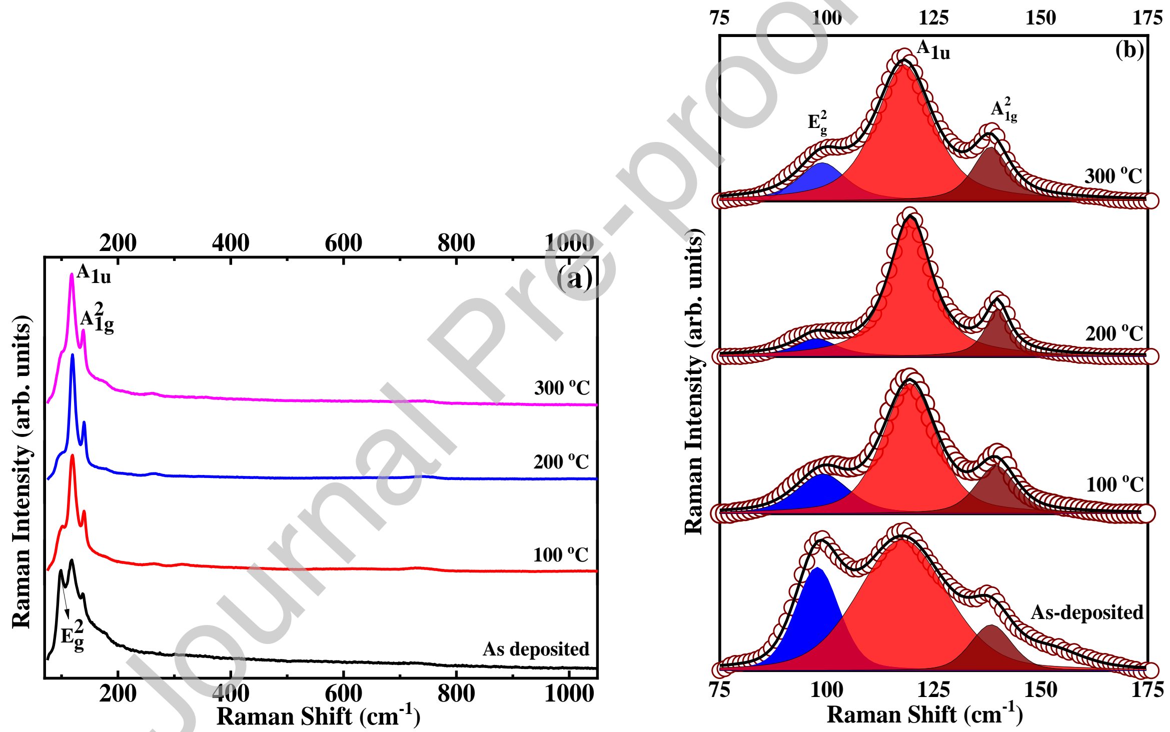

Journal Pre-proof

Figure 4: FESEM images of (a to d) cross sectional and (e to h) surface morphology images of as-deposited and post annealed Te-rich Bi_2Te_3 thin films. (a, e) as deposited; (b, f) 100 °C; (c, g) 200 °C; (d, h) 300 °C.

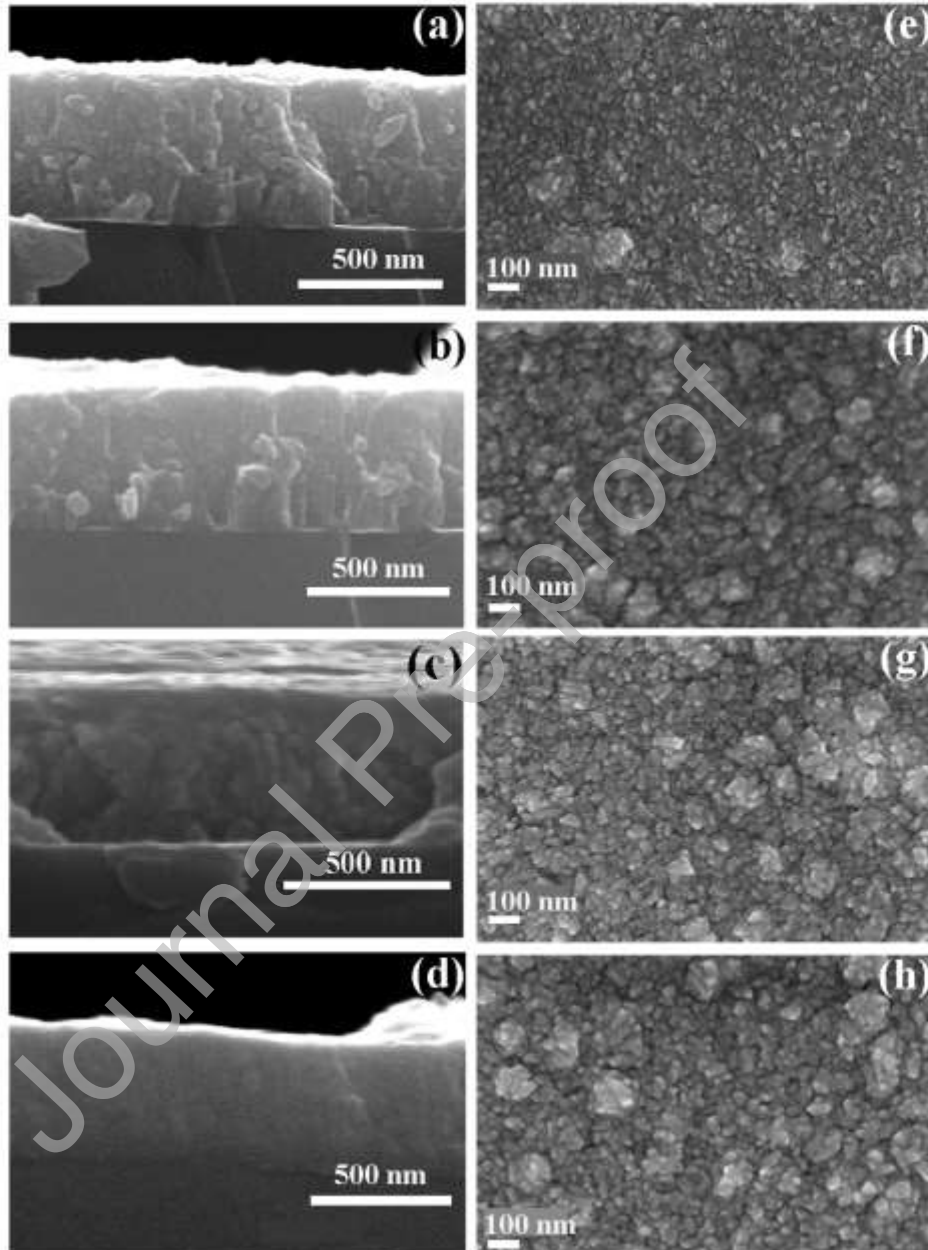

Journal Pre-proof

Figure 5: AFM images of as-deposited and post annealed Te-rich Bi_2Te_3 thin films. [(a) as-deposited, (b) 100 °C, (c) 200 °C and (d) 300 °C].

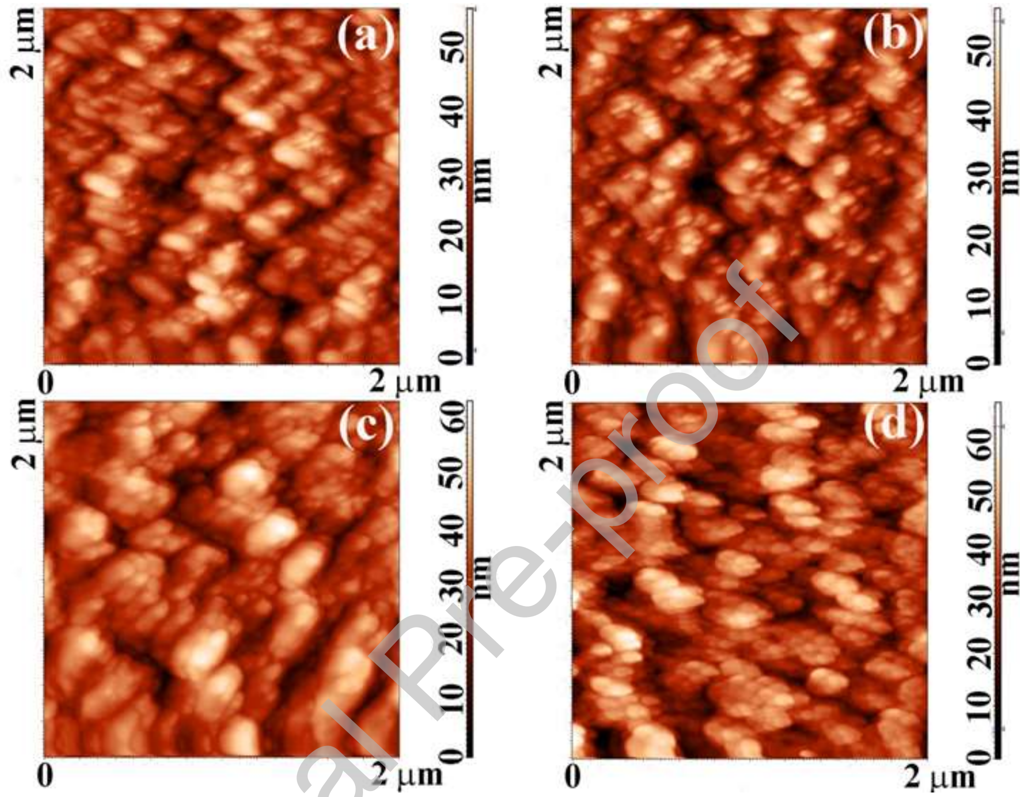

Journal Pre-proof

Figure 6: Bright field transmission electron microscopy images of as-deposited and post annealed Te-rich Bi_2Te_3 thin films: (a) as-deposited, (b) 100 °C, (c) 200 °C and (d) 300 °C. (e) to (h) are the SAED patterns of (a) to (d), respectively.

Journal Pre-proof

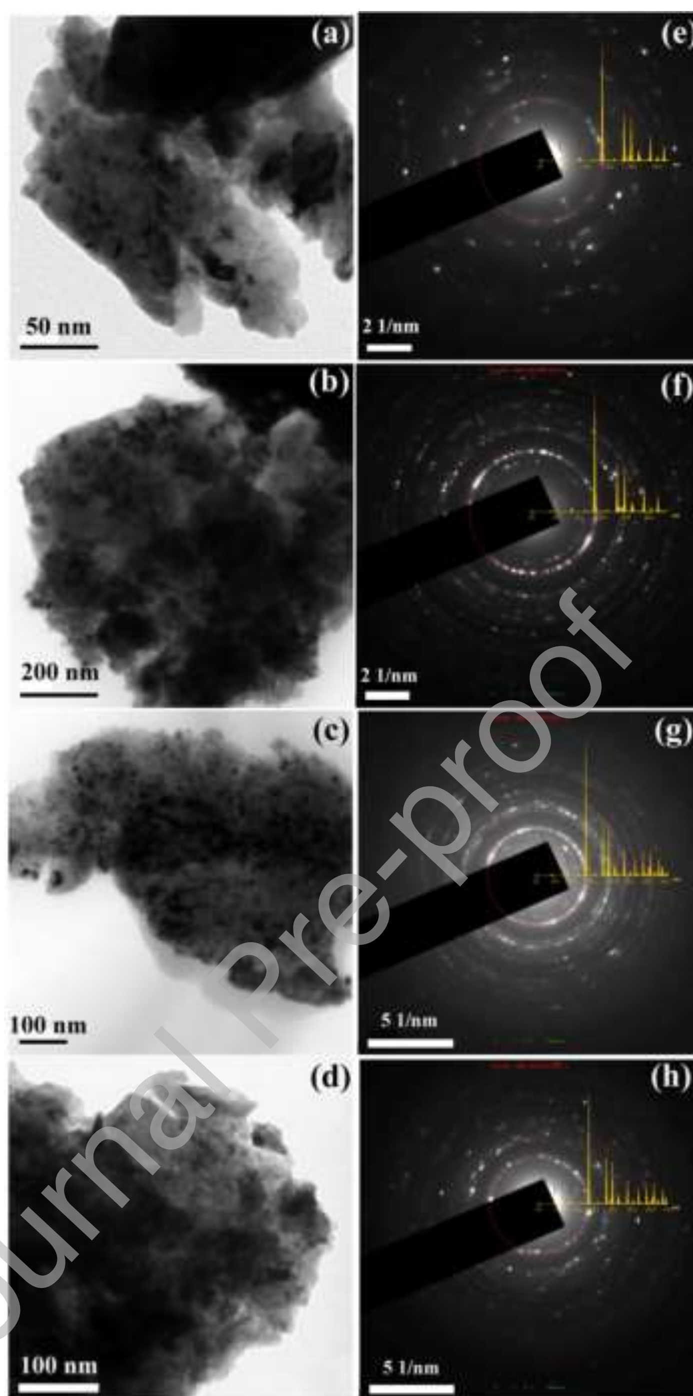

Journal Pre-proof

Figure 7: High resolution transmission electron microscopy images of as-deposited and post annealed Te-rich Bi_2Te_3 thin films. [(a) as-deposited, (b) 100 °C, (c) 200 °C and (d) 300 °C]. The white arrows in (d) show the planar defect regions.

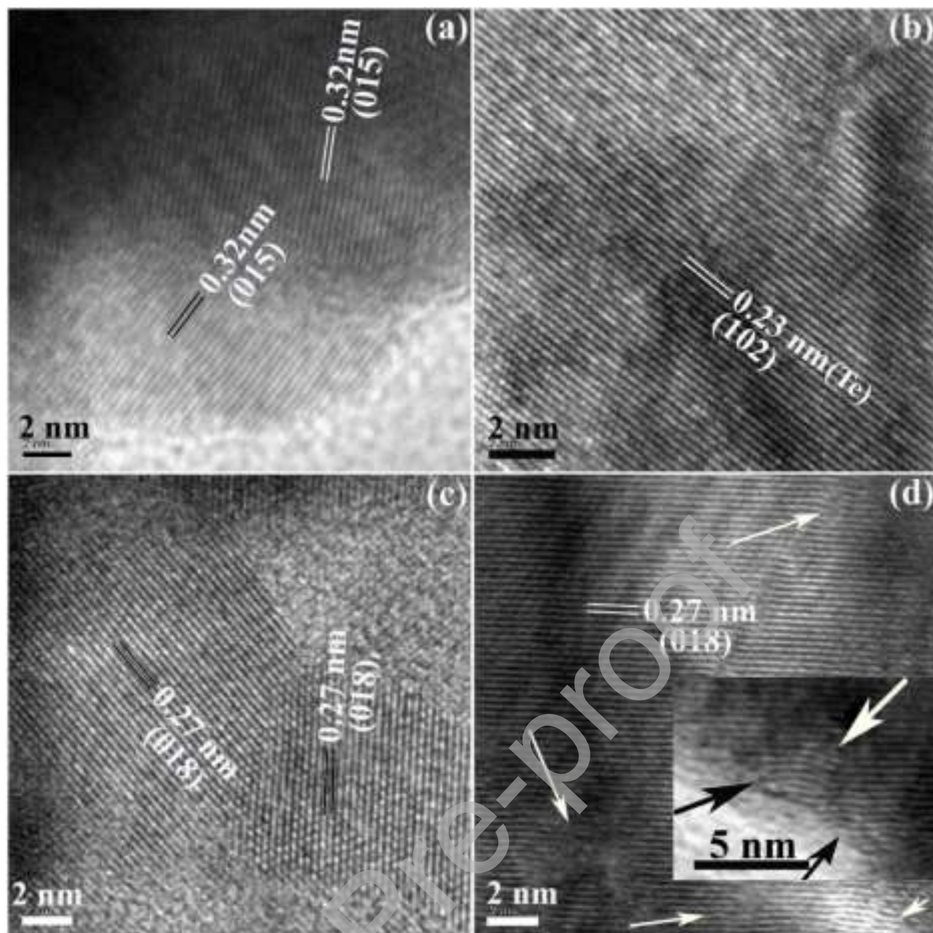

Journal Pre-proof

Figure 8: STEM image and EDS mapping of Bi and Te from the particles obtained from Te-rich Bi_2Te_3 thin films annealed at (A) 100 °C and (B) 200 °C. In the panel (C) line scans obtained from two regions marked in the STEM image given in (B) are shown.

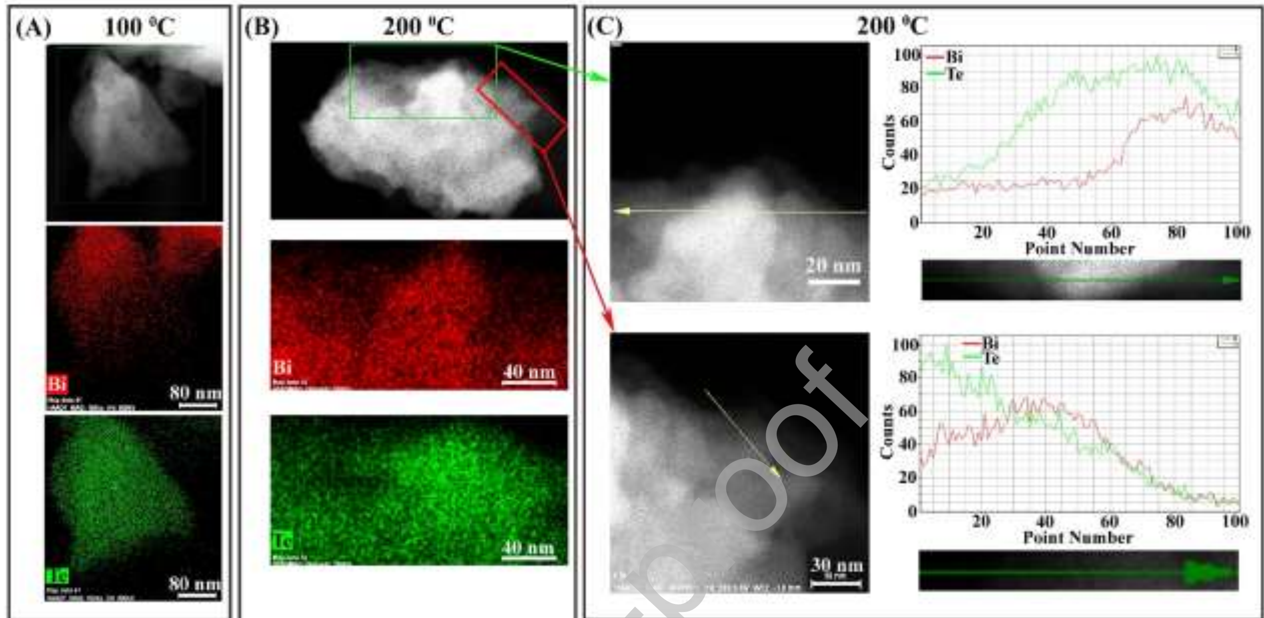

Journal Pre-proof

Journal Pre-proof

Figure 9: (a) Diffused reflection spectra of as-deposited Te-rich Bi_2Te_3 films and post annealed Te-rich Bi_2Te_3 thin films. (b) and (c) show the K-M transformed reflectance spectra of as-deposited and annealed at different temperatures for a direct and indirect band respectively.

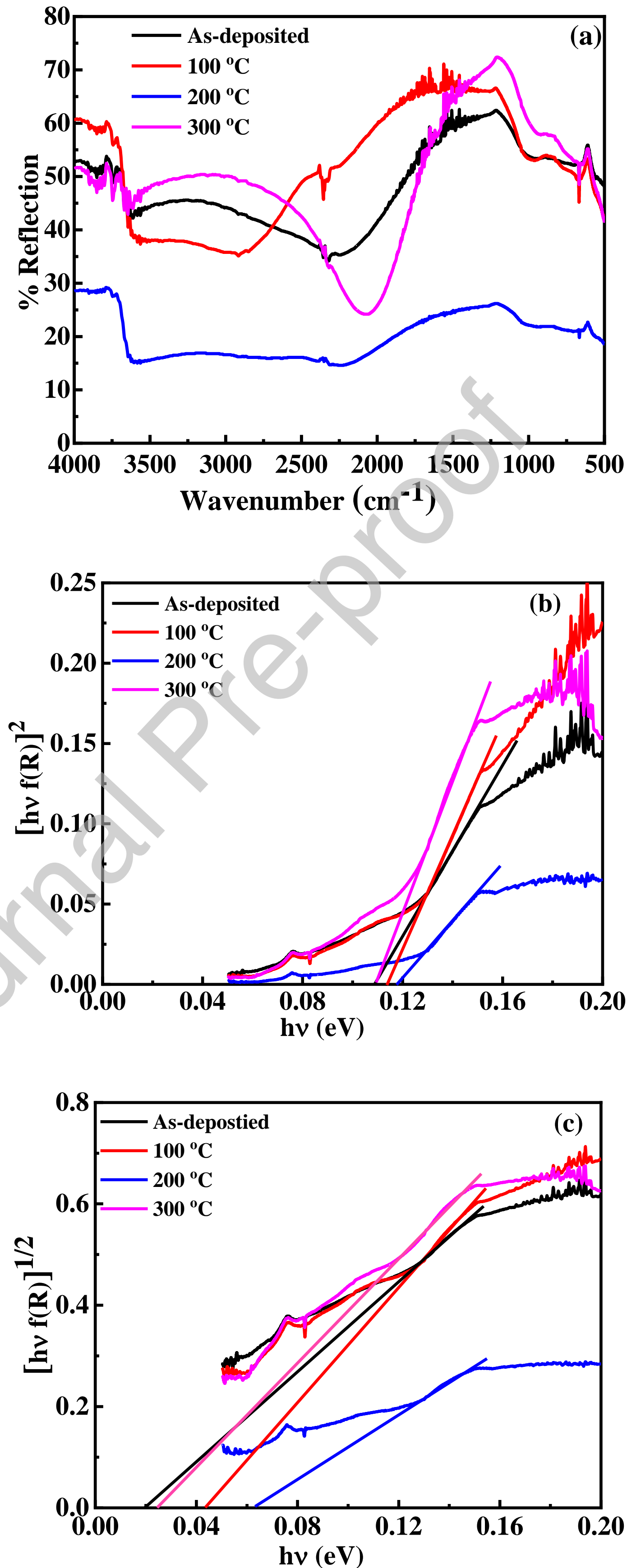

Journal Pre-proof

Figure 10: Carrier density and mobility of as-deposited and post annealed Te–rich Bi_2Te_3 thin films.

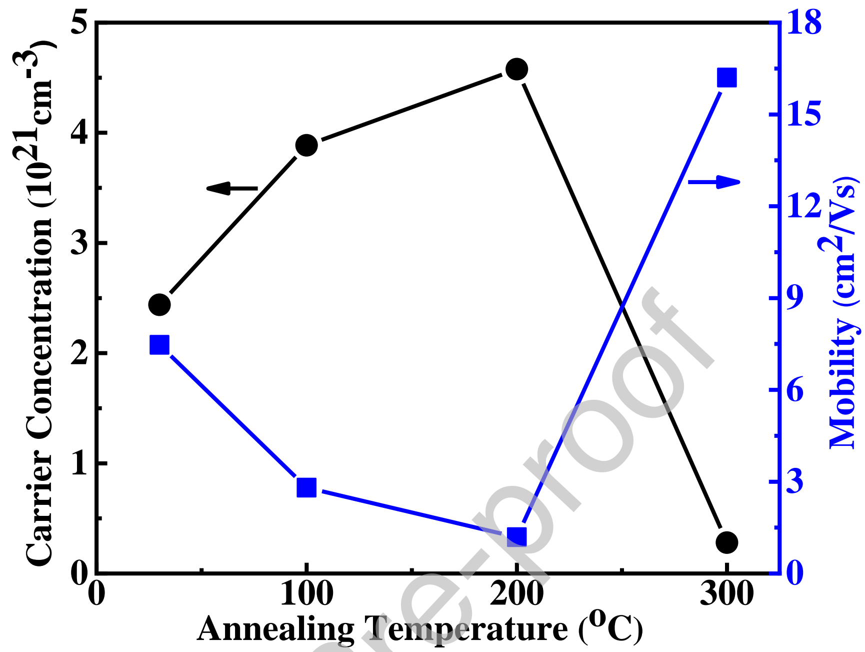

Journal Pre-proof

Journal Pre-proof

Figure 11: Temperature dependent resistivity of as-deposited and post annealed Te-rich Bi_2Te_3 thin films.

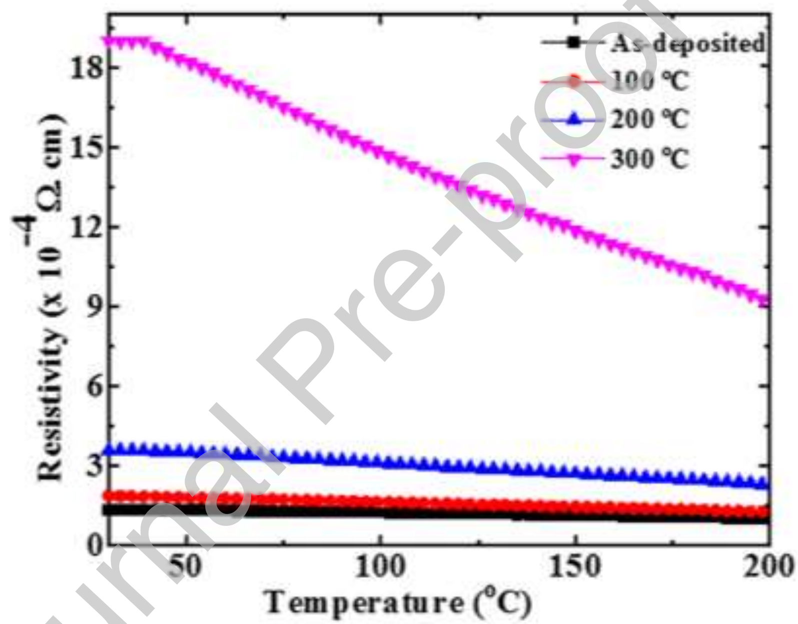

Journal Pre-proof

Journal Pre-proof

Figure 12: Electrical and thermoelectric properties of as-deposited and post annealed Te-rich Bi_2Te_3 thin films measured at room temperature.

Journal Pre-proof

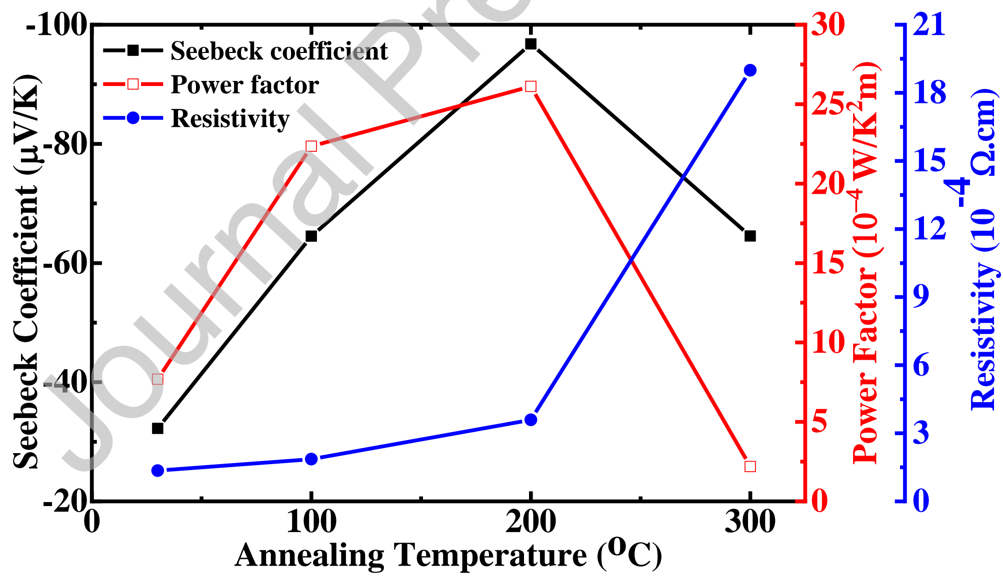

Journal Pre-proof

Figure 13: (a) The effect of applied temperature on Seebeck coefficient of as-deposited and post annealed Te-rich Bi_2Te_3 thin films. (b) The effect of applied temperature on power factor of Te-rich Bi_2Te_3 films.

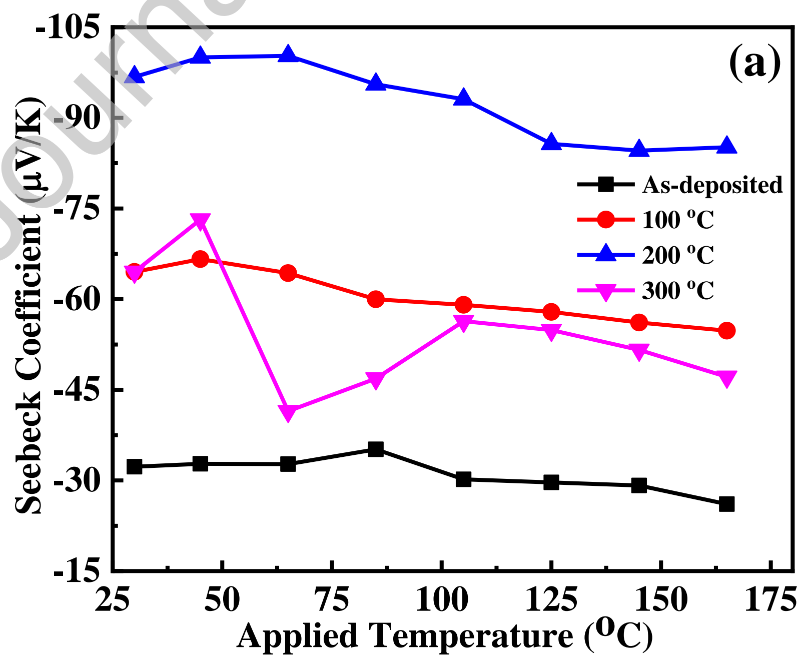

Journal Pre-proof

Journal Pre-proof

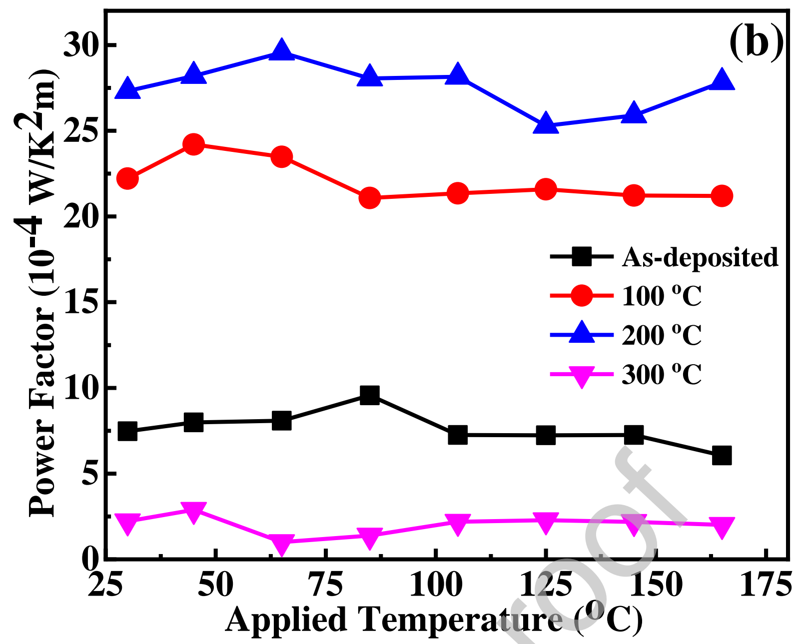

Journal Pre-proof

Journal Pre-proof

Table 1: Crystallite size, microstrain and structural lattice parameters estimated from the Rietveld refinements of the x-ray diffraction patterns of Te-rich Bi_2Te_3 thin films annealed for 1 h in vacuum (3×10^{-4} Pa). Estimated standard deviations are given in parentheses.

Te-rich Bi_2Te_3 thin film	Crystallite size ($d \pm 10$Å)	Micro strain (%)	Lattice parameter			Goodness of fit
			a (Å)	*c* (Å)	*c/a*	
As-deposited	131	0.066	4.3749(8)	30.0027(3)	6.858	1.26
100 °C	148	0.023	4.4156(3)	30.0259(6)	6.799	1.60
200 °C	189	0.048	4.4828(1)	30.4466(3)	6.792	1.70
300 °C	233	0.086	4.3939(3)	30.5558(6)	6.954	2.38

Journal Pre-proof

Journal Pre-proof

Table 2: Peak position and intensity ratio of Raman peaks in as deposited and annealed Te-rich Bi_2Te_3 thin films.

Te-rich Bi_2Te_3 thin film	Peak position			Line (Integrated) intensity ratio	
	E_g^2 (cm^{-1})	A_{1u} (cm^{-1})	A_{1g}^2 (cm^{-1})	$I(A_{1g}^2)/I(E_g^2)$	$I(A_{1u})/I(E_g^2)$
As-deposited	98.62	117.81	137.73	0.81 (0.43)	1.08 (2.52)
100 °C	99.39	119.05	139.69	1.96 (0.95)	2.25 (3.45)
200 °C	97.86	119.42	139.69	2.28 (1.63)	2.95 (8.09)
300 °C	99.39	117.80	138.19	2.20 (1.11)	2.15 (4.36)

Journal Pre-proof

Journal Pre-proof

Table 3: Composition form EDS, thickness from cross-sectional SEM, roughness from AFM and bandgap estimation from DRS studies of as deposited and annealed Te-rich Bi_2Te_3 thin films.

Te-rich Bi_2Te_3 thin film	*at.* % (± 0.5 %)		Thickness (± 5 nm)	Average Roughness (± 0.1 nm)	RMS Roughness (± 0.1 nm)	Direct Bandgap (± 0.004 eV)	Indirect Bandgap (± 0.004 eV)
	Bi	Te					
As-deposited	29.8	70.2	500	6.2	7.8	0.109	0.020
100 °C	22.1	77.9	486	6.4	7.9	0.114	0.043
200 °C	22.2	77.8	478	7.2	9.1	0.118	0.063
300 °C	28.9	71.1	473	7.7	9.7	0.109	0.024

Journal Pre-proof

Credit Author Statement:

C. Sudarshan: Conceptualization, Methodology, Investigation, Data curation, Visualization, Formal analysis, Writing - original draft, Project administration, Resources.

S. Jayakumar: Resources, Formal analysis, Writing - review & editing, Supervision.

K. Vaideki: Supervision, Writing - review & editing.

C. Sudakar: Methodology, Resources, Formal Analysis, Writing - review & editing.

Journal Pre-proof

Journal Pre-proof

Declaration of interests

☒ The authors declare that they have no known competing financial interests or personal relationships that could have appeared to influence the work reported in this paper.

☐The authors declare the following financial interests/personal relationships which may be considered as potential competing interests:

Journal Pre-proof